APPLIED SCIENCES AND ENGINEERING

Achieving symmetric snap-through buckling via designed magnetic actuation

Yingchao Zhang[1,2], Weicheng Huang[3], Mingchao Liu[4], Jing Yu[2,5]*, Huajian Gao[2,5]*

Copyright © 2025 The Authors, some rights reserved; exclusive licensee American Association for the Advancement of Science. No claim to original U.S. Government Works. Distributed under a Creative Commons Attribution NonCommercial License 4.0 (CC BY-NC).

Symmetric snap-through buckling, although both theoretically achievable and practically advantageous, has remained rare in bistable systems, with most studies favoring asymmetric snapping due to its lower energy barrier. Previous observations of symmetric snapping have been limited to high loading rates. In this work, we present a universal strategy to achieve symmetric snapping under quasi-static conditions by designing magnetization (M)–interface patterns that effectively suppress asymmetric modes. A simplified theoretical model demonstrates that this behavior results from the interplay between pitchfork and saddle-node bifurcations, with predictions validated through simulations and experiments using hard magnetic elastomers. Resisting forces generated by multiple M-interfaces counteract asymmetric snapping, enabling distinct symmetric configurations. Extending this approach to higher-order symmetric snapping, we uncover a quasi-linear scaling law between critical fields and snapping order. These findings establish a robust framework for designing snapping systems with enhanced control and predictability, as demonstrated by a mechanical-magnetic snapping switch, paving the way for advanced applications in precision engineering and magnetic-mechanical actuation.

INTRODUCTION

Picture the delicate yet swift closure of a Venus flytrap's leaves as it captures its prey (*1*, *2*) or the marked inversion of an umbrella under a sudden gust of wind. Both phenomena showcase the captivating mechanics of elastic snap-through buckling, a sudden transition between two stable equilibrium states. Beyond their natural elegance, these rapid transitions have inspired innovative, energy-efficient designs for applications such as microelectromechanical system switches (*3*, *4*), jumping robots (*5*–*8*), metamaterial-based devices (*9*–*15*), and energy-harvesting devices (*16*, *17*).

Among various bistable structures, Euler buckling–based systems are widely adopted as models due to their simplicity, universality, and material independence. Consider gently compressing a slender strip of paper: It naturally buckles into one of two stable states, either upward or downward, forming mirror-symmetric configurations. Each state also exhibits left-right symmetry about the axis passing through its geometric midpoint when identical boundary conditions are applied at both ends. Transitions between these states can be triggered mechanically, such as by applying a point force to the arch (*18*, *19*), or remotely actuated using magnetic or photomechanical fields in active materials (*20*–*23*).

Symmetry is a fundamental principle in physics, shaping energy landscapes and governing equilibrium across diverse systems, ranging from condensed matter to biological (*24*, *25*). However, preserving symmetry often demands substantial energy expenditure. The snap-through buckling illustrates this challenge. Beyond its theoretical significance, symmetry plays a practical role in applications where symmetric snapping offers superior control and predictability compared to asymmetric modes. However, despite intrinsic symmetry in geometry, boundary conditions, and actuation fields, transition configurations often deviate from left-right symmetry. Asymmetric snap-through is commonly observed as the default mode due to its lower energy barrier, making it the energetically preferred pathway. While symmetric snap-through is theoretically feasible, it was only recently demonstrated under sufficiently high loading rates (*26*), remaining an intriguing but constrained phenomenon. To date, symmetric snapping under quasi-static conditions, a critical requirement for many real-world applications, has yet to be realized.

Here, we present a universal strategy to control snapping modes, with a particular focus on enabling symmetric modes by suppressing all asymmetric ones. Combining experiments, simulations, and theoretical analysis, we document the occurrence of symmetric snapping under quasi-static conditions, uncovering the underlying mechanisms and establishing a robust framework for designing snapping systems with enhanced functionality.

RESULTS

Bistable model system

As illustrated in Fig. 1A (a), we examine the snapping behavior of an elastica structure composed of hard ferromagnetic soft elastomers (HME), a class of active materials consisting of hard ferromagnetic particles (MPs) embedded within a soft elastomer matrix (*27*–*35*). The key to achieving different snapping modes lies in the design of the magnetization (**M**) distribution along the elastica's length, accomplished through a fold [Fig. 1A (b)], pre-magnetization [Fig. 1A (c)], and unfolding (Materials and Methods and the Supplementary Materials). At specific fold positions ($s = s_i$), referred to as M-interface, regions with reversed remanent **M** are introduced [Fig. 1A (d)]. The alternating orientation of **M** is expressed as $\mathbf{M}_i = (-1)^{i+1} M \mathbf{e}_x$ for $s \in [s_{i-1}, s_i]$, where M is the magnitude of **M**, $\mathbf{e}_x$ is the direction along elastica's length, and $i = 1, \ldots, N+1$ corresponds to segments defined by N M-interfaces.

We consider a bistable system formed by Euler buckling of an elastica clamped at both ends, with varying numbers of M-interface: single-M, triple-M, and five-M configurations (Fig. 1B). An initial

[1]School of Materials Science and Engineering, Nanyang Technological University, Singapore 639798, Singapore. [2]Applied Mechanics Laboratory, Department of Engineering Mechanics, Tsinghua University, Beijing 100084, China. [3]School of Engineering, Newcastle University, Newcastle upon Tyne NE1 7RU, UK. [4]Department of Mechanical Engineering, University of Birmingham, Birmingham B15 2TT, UK. [5]Mechano-X Institute, Tsinghua University, Beijing 100084, China.
*Corresponding author. Email: yu-jing@tsinghua.edu.cn (J.Y.); gao.huajian@tsinghua.edu.cn (H.G.)

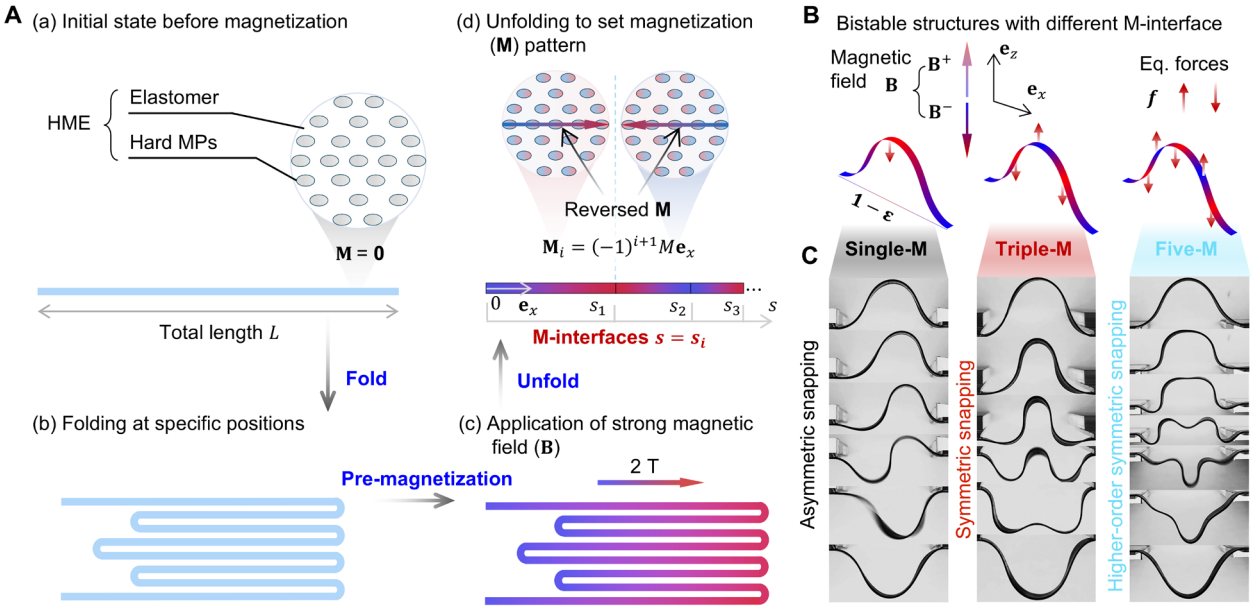

Fig. 1. Model system and snapping modes overview. (**A**) Schematic representation of the hard ferromagnetic soft elastomer (HME), consisting of an elastomer matrix embedded with hard ferromagnetic particles (MPs). (a to d) Method for fabricating magnetization (**M**) distributions in HME. The process involves three steps: (b) folding the elastica at specific positions, (c) applying a strong magnetic field to pre-magnetize the folded sample, and (d) unfolding the sample to create the desired magnetization pattern along its length and featuring designed magnetization interfaces at positions $s = s_i$. (**B**) Bistable structures with single-M, triple-M, and five-M configurations, formed through Euler buckling under end-to-end shortening ε. A uniform magnetic field **B** applied either along ($\mathbf{B}^+$) or opposite ($\mathbf{B}^-$) $\mathbf{e}_z$ triggers snapping, with equivalent (Eq.) point forces at the M-interfaces. (**C**) Representative snapping modes: asymmetric snapping for the single-M configuration (left), symmetric snapping for the triple-M configuration (middle), and higher-order symmetric snapping for the five-M configuration (right). The images are selected to highlight key moments of the snapping behavior and do not correspond to uniform time intervals. The complete snapping processes are documented in real time in movies S1 to S3.

end-to-end shortening, $\varepsilon = \Delta L/L$, creates bistable structures in all three cases. A remote, spatially uniform external magnetic field **B** is used to trigger the snapping. Depending on its orientation, the field has two configurations: $\mathbf{B} = B^+\mathbf{e}_z$ (aligns along $\mathbf{e}_z$) or $\mathbf{B} = -B^-\mathbf{e}_z$ (aligns opposite $\mathbf{e}_z$), where B^+ and B^- denote the absolute field strengths. These are referred to as the $\mathbf{B}^+$-stimuli and $\mathbf{B}^-$-stimuli, respectively, and collectively as the **B**-stimuli. We demonstrated that the deformation of a uniform HME-based elastica under **B**-stimuli is equivalent to that under point forces ($\boldsymbol{f}$) applied at the M-interfaces (section S1). The equivalent force, expressed in nondimensional form, is given by $\boldsymbol{f}_i = (-1)^{i+1} 2AMBL^2 / EI\mathbf{e}_z$, where A is the elastica's cross-sectional area, L is the total length, EI is the bending stiffness, and B is the magnetic field strength corresponding to B^+ or $-B^-$. This equivalence provides an intuitive understanding of the system behavior while highlighting the advantages of magnetic actuation, such as remote and contactless actuation, and high-power density, making it a powerful tool for triggering snapping transitions (*20*, *27*).

Different designs for the number and positions of M-interfaces result in distinct snapping modes (Fig. 1C). For the single-M system, the upward-buckled elastica snaps asymmetrically to the inverted state upon **B**-stimuli (Fig. 1C, left, and movie S1), despite the system's inherent symmetry. This behavior is consistent with both our findings and previous studies (*18*, *20*, *22*, *36*). The triple-M design enables symmetric snapping (Fig. 1C, middle, and movie S2), where the elastica maintains symmetry throughout the snap-through process. The five-M configuration further achieves higher-order symmetric snapping modes (Fig. 1C, right, and movie S3), where the number of inflection points, locations where the curvature vanishes, characterizes the snapping order (see section S1 for a rigorous definition). The realization of these modes is strongly influenced by not only the number but also the positions of the M-interfaces.

This progression raises several fundamental questions. First, why does asymmetric snapping dominate in the single-M system, whereas symmetric and higher-order symmetric modes emerge in the triple-M and five-M systems? Second, what are the rational design criteria for achieving symmetric and higher-order symmetric snapping modes? Third, how are these distinct modes interconnected? Last, is our strategy universally applicable to other bistable systems?

Phasing out asymmetric mode

Exploring the entire design space of M-interface positions to achieve symmetric snapping through simulations or experiments, while feasible, lacks a clear direction. Therefore, a simple theoretical model is crucial for revealing the underlying physics and guiding this search. The deformation of the elastica is governed by the Kirchhoff model for large ε and reduce to the Foppl–von Karman (FvK) model for small ε with shallow deflections. For the triple-M configuration, the nondimensional deflection W_i in each segment is described as piecewise functions separated by M-interfaces (section S1)

$$W_i = A_{ij} w_j, \text{for } X \in [X_{i-1}, X_i] \quad (1)$$

where $w_j = [1, X, \cos\lambda X, \sin\lambda X]^{\mathrm{T}}$ represents the basis functions and A_{ij} are the coefficients specific to each segment. Boundary conditions at both ends along with continuity conditions at the M-interfaces establish relationships among A_{ij}, ultimately leading to the eigenvalue equation

$$\mathbf{K}\boldsymbol{\Lambda} = \mathbf{0} \tag{2}$$

where $\mathbf{K}$ depends on X_i and λ. The vector $\boldsymbol{\Lambda}$ is a rearranged form of A_{ij}, compactly expressed as $\Lambda_i = A_{1i} + (-1)^i A_{4i}$, and $\Lambda_{i+4} = A_{2i} + (-1)^i A_{3i}$ for $i = 1 \sim 4$. For $\boldsymbol{\Lambda} = \mathbf{0}$, the coefficients of the even terms in Eq. 1 are identical, while those of the odd terms are opposite, yielding $W(X)$ as a symmetric function corresponding to a symmetric deformation mode. Conversely, if $\boldsymbol{\Lambda} \neq \mathbf{0}$ with $\det\left[\mathbf{K}\left(X_i, \lambda\right)\right] = 0$, then the system admits an asymmetric mode, yielding $\lambda_0 \approx 8.99$, consistent with previous results (*18*). This critical value is independent of the number or positions of M-interfaces. With λ_0 determined, the relationship between the **B**-stimuli and deflection in the asymmetric branch can be derived. This relationship, notably linear and dependent on the positions of M-interfaces, allows us to define the stiffness of the asymmetric mode as $k = dB/d\delta$, where $\delta = W_0(0) - W_0$ is the midpoint vertical displacement in response to **B**-stimuli and W_0 the nondimensional midpoint deflection. For the triple-M configuration, we have

$$k = -\frac{4\lambda_0^3 \cos\lambda_0/4}{\lambda_0(1-2\mu)\cos\lambda_0/4 - 4\sin\lambda_0(1-2\mu)/4} \tag{3}$$

where a rescaling parameter μ, spanning the range [0, 1], denotes the position of the first M-interface ($S = \mu/2$), with $S = s/L$ representing the nondimensional arclength, as illustrated at the top of Fig. 2A. When $\mu = 0$ (or 1), the system reduces to single-M under $\mathbf{B}^+$(or $\mathbf{B}^-$). Notably, as $\mu \to 0.5$, the stiffness diverges to infinity, making the asymmetric mode energetically unfavorable. Given the similarity between $\mathbf{B}^+$ and $\mathbf{B}^-$, we focus on $\mathbf{B}^-$ for further illustration.

The $B^- \sim \delta$ relationship for various μ values demonstrates that decreasing μ from 1.0 to 0.5 significantly increases stiffness (Fig. 2A).

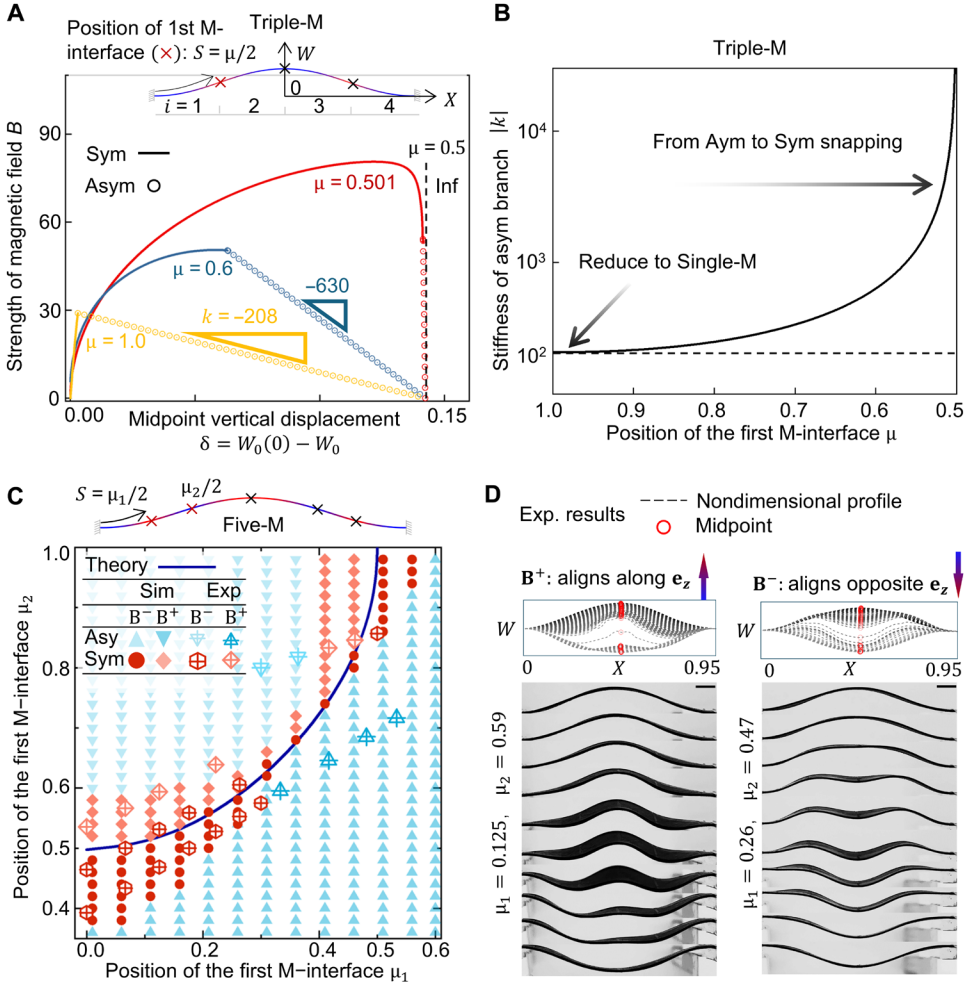

Fig. 2. Phasing out asymmetric branch to achieve symmetric snapping. (**A**) The B-δ relationships for the triple-M configuration are shown for various positions of the first M-interface ($S = \mu/2$). In this load-controlled system, the midpoint vertical displacement δ is plotted on the horizontal axis to intuitively illustrate the stiffness of the asymmetric branch through the slope of the curve. (**B**) The stiffness of asymmetric branch k versus μ. As μ approaches 0.5, the stiffness of the asymmetric branch diverges, phasing out the asymmetric branch. (**C**) Phase diagram in the $\mu_1 - \mu_2$ plane and representative experiments for the five-M configuration, where μ_1 and μ_2 denote the positions of the first ($S = \mu_1/2$) and second ($S = \mu_2/2$) M-interfaces, respectively. The solid line in (C) indicates the boundary where asymmetric branch phases out, as its stiffness diverges ($k_5 \to \infty$). Experimental and simulation results confirm symmetric snapping along this boundary. (**D**) Representative experimental results ($\varepsilon = 5\%$) for $\mathbf{B}^+$(left, $\mu_2 = 0.59$) and $\mathbf{B}^-$ (right, $\mu_2 = 0.47$) with $\mu_1 = 0.125$ align well with theoretical predictions. The images are selected to highlight key moments of the snapping behavior and do not correspond to uniform time intervals. The complete snapping processes are documented in real time in movies S4 and S5. Asy, asymmetric snapping; Sym, symmetric snapping; Sim, simulation results; Exp, experimental results.

In traditional midpoint loading (e.g., $\mu = 1$), the asymmetric branch has low stiffness, allowing it to intersect easily with the symmetric branch, making it the default pathway. By contrast, decreasing μ raises the stiffness of the asymmetric branch significantly (Fig. 2B), phasing it out and promoting symmetric snapping. This behavior is independent of ε.

The same principle extends to the five-M configuration, where the stiffness of the asymmetric branch depends on both the first ($S = \mu_1/2$) and second ($S = \mu_2/2$) positions of the M-interfaces, expressed as $k_5 = k_5(\mu_1, \mu_2)$. Here, μ_1 and μ_2 are rescaling parameters spanning [0, 1] in the five-M configuration, with $\mu_2 \geq \mu_1$, as depicted at the top of Fig. 2C. The boundary line, where $k_5 \to \infty$, delineates a region near which the asymmetric mode is phased out. This boundary, shown in Fig. 2C, reduces to the triple-M case when either $\mu_1 = 0$ or $\mu_2 = 1$,offering a direct extension of the principle. This theoretical insight effectively guides the search for achieving symmetric snapping in five-M systems.

Both simulations and experiments validate this prediction, as symmetric modes are observed along the boundary line $k_5(\mu_1, \mu_2) = \infty$ (Fig. 2C). Additionally, this boundary separates the snapping spaces for $\mathbf{B}^+$ and $\mathbf{B}^-$: Snapping occurs in the bottom-right corner for $\mathbf{B}^-$, while the opposite region corresponds to $\mathbf{B}^+$. Representative experimental results with same $\mu_1 = 0.125$ for $\mathbf{B}^+$ ($\mu_2 = 0.59$) and $\mathbf{B}^-$ ($\mu_2 = 0.47$) are shown in Fig. 2D and movies S4 and S5, demonstrating excellent agreement with theoretical predictions.

Competition between pitchfork and saddle node bifurcations

Building on our previous analysis, we now identify the phase boundary separating symmetric and asymmetric snapping modes. For snapping actuated by magnetic field, characterized as a "load"-controlled system, the phase boundary is determined by ensuring that the asymmetric branch emerges after the symmetric branch. The asymmetric branch corresponds to a pitchfork bifurcation, while the symmetric branch arises from a saddle-node bifurcation (*24*, *37*). The competition between these two bifurcation types defines the phase boundary.

To illustrate this concept, we focus on $\mathbf{B}^-$-stimuli and increase ε to 20%, adopting Kirchhoff model for improved accuracy at large deformations. As shown in Fig. 3A, when $\mu = 0.9$, close to the single-M configuration, the pitchfork bifurcation (asymmetric branch) precedes the saddle-node bifurcation, leading to asymmetric snapping as B^- increases. Conversely, at $\mu = 0.51$, near $\mu = 0.5$ (where the k diverges), the saddle-node bifurcation (symmetric branch) occurs first, resulting in symmetric snapping. The critical condition arises when the pitchfork and saddle-node bifurcations merge, defining the critical M-interface positions $\mu_c^{\pm}$ for $\mathbf{B}^{\pm}$.

The phase diagram in the $\mu - \varepsilon$ plane (Fig. 3B) reveals key observations. First, the FvK model predicts a constant critical M-interface position ($\mu_c^{\pm} \approx 0.62$) that is independent of ε. In contrast, the more accurate Kirchhoff model shows a nonlinear relationship between $\mu_c^{\pm}$ and ε, where larger ε broadens symmetric snapping region. This phenomenon is attributed to the high nonlinearity introduced by deep Euler buckling. Second, finite element method (FEM) simulations were performed to validate the theoretical predictions by incorporating imperfections, achieved by slightly shifting the second M-interface position away from the geometric midpoint (section S2). Including imperfections not only accounts for inevitable experimental deviations but also ensures a more robust phase diagram by mitigating numerical errors. The boundary lines obtained from simulations, shown as dash-dot lines in Fig. 3B, reveal that imperfections narrow the symmetric snapping region, although the overall trend between $\mu_c^{\pm}$ and ε remains consistent.

Experiments further validate these findings, showing excellent agreement with theoretical predictions (Fig. 3C, additional examples are in the Supplementary Materials). Monitoring snapping process under **B**-stimuli, we measure the rotation angle at the geometric midpoint (θ_{mid}) versus the loading frame. For cases within the symmetric snapping space ($\mu_c^- < \mu < \mu_c^+$, e.g., $\mu = 0.48$ or 0.53), θ_{mid} remains near zero, despite slight deviations from imperfections, indicating dominant symmetric snapping. Conversely, outside the symmetric space ($\mu = 0.23$), θ_{mid} increases significantly at snapping point, confirming asymmetric snapping.

An intuitive explanation for these behaviors is illustrated in Fig. 3C (right). In the single-M or traditional snapping systems, a single equivalent driving force triggers snapping (bottom left). Although the system is inherently symmetric, its evolution is highly sensitive to imperfections, causing the structure to swing left or right. This observation aligns with recent studies (*26*). In contrast, the multiple M-interface design in our system introduces several equivalent point forces under **B**-stimuli (middle left and top). For the triple-M configuration, either $\mathbf{B}^+$ or $\mathbf{B}^-$ induces at least one driving force ($\mathbf{B}^+$) and one resisting force ($\mathbf{B}^-$). The driving force initiates snapping, while the resisting force counteracts both snapping and asymmetric modes. For $\mathbf{B}^-$-stimuli, a single resisting force at the midpoint produces a "W"-like symmetric snapping shape (top left). Conversely, for $\mathbf{B}^+$-stimuli, two resisting forces located symmetrically on either side of the midpoint result in an "M"-like snapping shape (middle left).

Phase diagram for five-M configuration

Building on the established principle of bifurcation competition, we extend our analysis to the five-M configuration through the phase diagram (Fig. 4A). For small ε, the phase diagram is independent of ε, similar to the triple-M configuration. For deeper arcs, the Kirchhoff model provides more accurate results but follows a similar trend. Detailed comparisons between models provided in section S1. Here, we focus on the FvK model for simplicity. Dashed lines highlight transitions between symmetric and asymmetric snapping modes. The colormap represents the critical magnetic field B_c required to trigger snapping at $\varepsilon = 10\,\%$.

The phase diagram reveals distinct regions. Near $\mu_1 = \mu_2$ under $\mathbf{B}^-$ (or $\mu_1 = 0$ and $\mu_2 = 1.0$ under $\mathbf{B}^+$), the system reduces to single-M behavior. In this region, snapping is dominated by driving forces located near the midpoint, with negligible resisting forces, resulting in asymmetric snapping. Moving toward the symmetric region, a transition zone with increased B_c is observed, where asymmetric snapping still dominates. Entering the symmetric region requires stronger fields due to the interplay of driving and resisting forces. Cases where $\mu_1 = 0$ or $\mu_2 = 1.0$ fully reduce to triple-M behavior.

To complement traditional static FEM simulations, we used the recently developed discrete magnetic rod (DMR) method to investigate the dynamic behavior of the snapping process (section S2). The simulation details for the snap-through process are similar to recent studies (*26*), with modifications to incorporate magnetic actuation in the five-M system (*35*). This approach provides cross-validation for our results. As shown in Fig. 4B, we plot the maximum θ_{mid} against μ_1 and μ_2. Consistent with FEM simulation

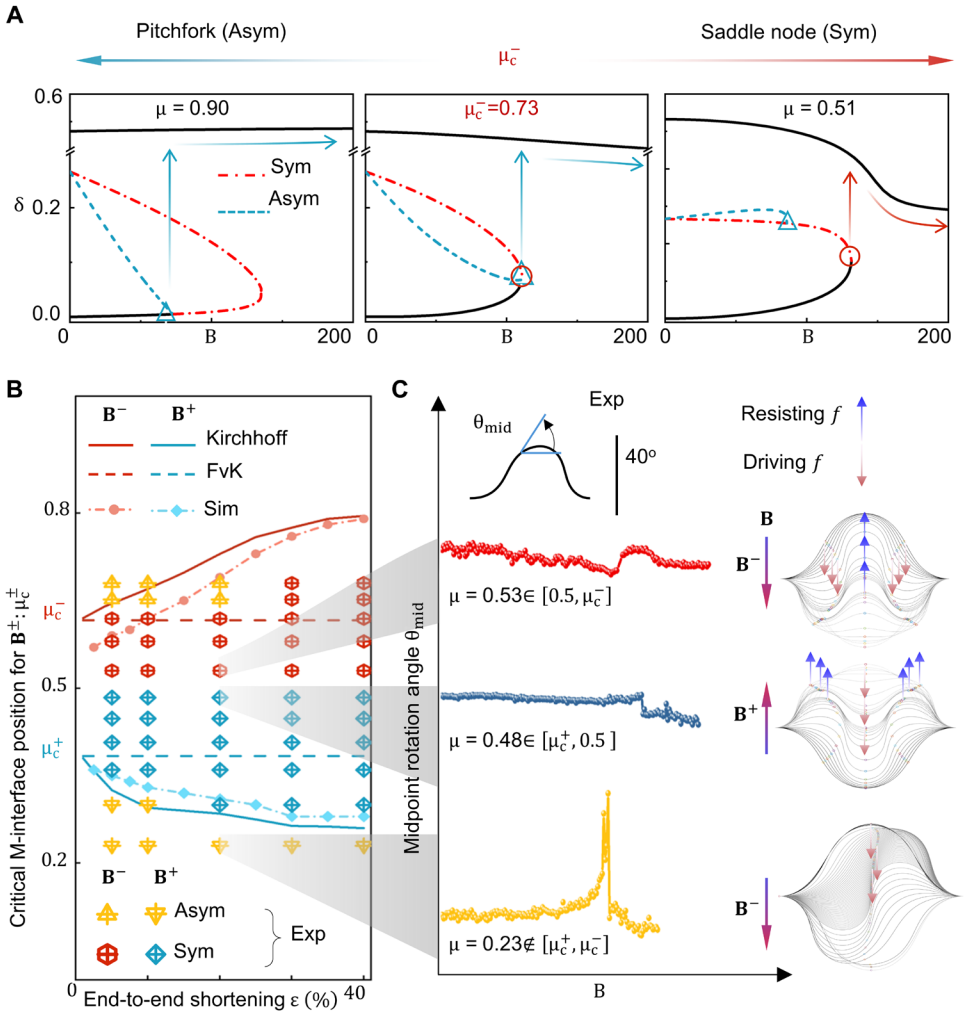

Fig. 3. Bifurcation and phase diagrams for the triple-M configuration. (**A**) Bifurcation diagrams showing the transition from a pitchfork bifurcation (μ = 0.9) to a saddle-node bifurcation (μ = 0.51) as the M-interface position (μ) approaches the stiffness divergence boundary. (**B**) Phase diagram in the μ − ε plane. The FvK model predicts constant critical positions ($\mu_c^{\pm} \approx 0.62$), while the Kirchhoff model reveals nonlinear boundaries (solid lines). Dash-dot lines indicate finite element method (FEM) simulation results. (**C**) Experimental results and intuitive explanation. The left panel plots midpoint rotation angles versus loading frame for symmetric snapping (μ = 0.48 and 0.53) and asymmetric snapping (μ = 0.23). The right panel illustrates the competition between driving and resisting forces: $\mathbf{B}^-$ produces a W-like shape, $\mathbf{B}^+$ forms an M-like shape, and single-M lacks resisting forces, resulting in asymmetric snapping ("S"-like shape). The images are selected to highlight key moments of the snapping behavior and do not correspond to uniform time intervals. The complete snapping processes are documented in real time in movies S6 to S8.

results, a notable drop in $\max\theta_{mid}$ is observed as μ_1 and μ_2 approach the phase boundaries, indicating the onset of symmetric snapping. Further quantitative comparison between DMR simulation results and the theoretical model is presented in Fig. 4C, demonstrating excellent agreement.

Within the symmetric snapping region, a subregion characterized by significantly larger B_c is identified (Fig. 4A, red markers). For the triple-M configuration, symmetric snapping involves up to four inflection points, corresponding to the W- or M-like shapes, referred to as fourth-order symmetric snapping ($\mathcal{N} = 4$). However, in five-M systems near $\mu_1 \approx 0.3$ and $\mu_2 \approx 0.6$, all five M-interfaces play non-neglectable roles. This heightened competition between resisting and driving forces leads to multiple inflection points before snapping, a phenomenon that we define as higher-order symmetric snapping. To quantify this, the rotation angle $\theta(S)$ is expanded as a finite series of buckling modes (section S1.4)

$$\theta = \sum_{i=1}^{\mathbb{N}} \mathcal{A}_i \sin i\pi S, \mathcal{A}_i = 2\int_0^1 \theta \sin i\pi S dS \quad (4)$$

where $\mathcal{A}_i$ represents the amplitude of the ith mode. Odd modes represent asymmetric contributions, while even modes correspond to symmetric contributions. For symmetric snapping in the triple-M configuration, $\mathcal{A}_2$ and $\mathcal{A}_4$ dominate. For higher-order symmetric snapping, higher-order terms $\mathcal{A}_6$ and $\mathcal{A}_8$ must also contribute significantly. We define the order ratio as

$$\mathcal{O} = \max\{|\mathcal{A}_6|, |\mathcal{A}_8|\} / \max\{|\mathcal{A}_2|, |\mathcal{A}_4|\} \quad (5)$$

and higher-order symmetric snapping is classified when $\mathcal{O} \geq 50\%$. Using this criterion, higher-order regions are identified in Fig. 4A, with representative experimental images provided in Fig. 4 (D and E) (see movies S8 and S9). The phase diagram is thus divided into

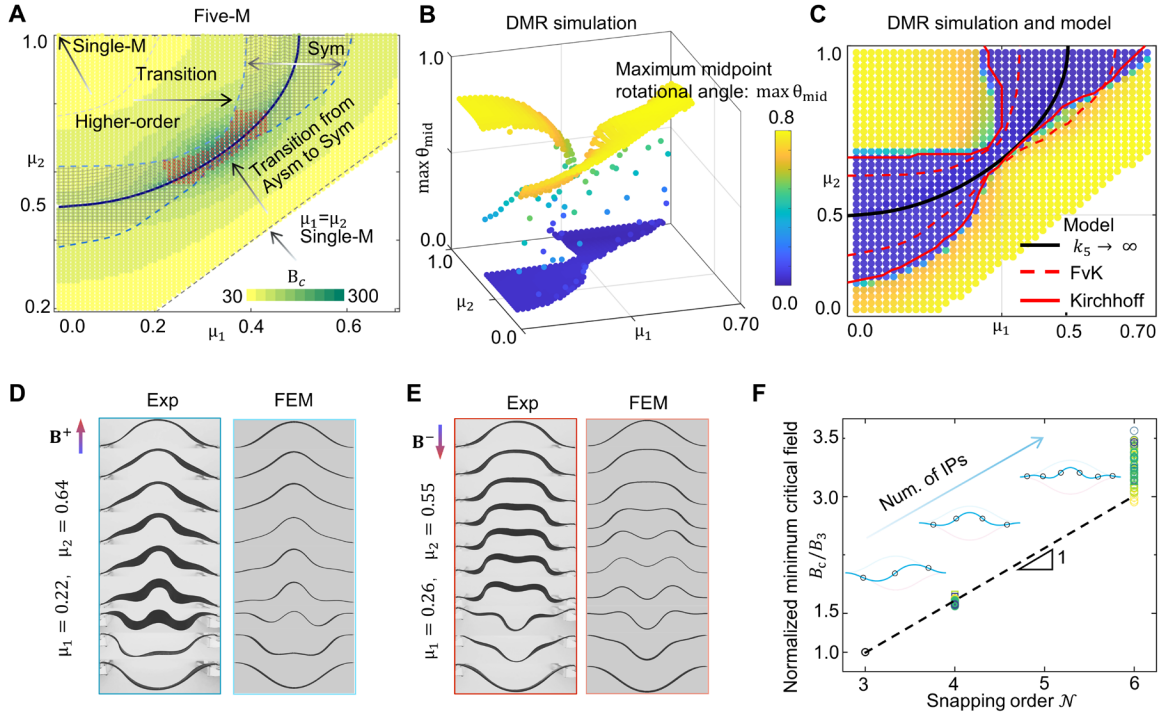

Fig. 4. Phase diagram for the five-M configuration and scaling laws across snapping modes. (**A**) Phase diagram for $\varepsilon = 10\%$, showing regions for asymmetric, symmetric (black markers), and higher-order symmetric snapping (red markers). The colormap represents the critical magnetic field B_c required to trigger snapping. (**B** and **C**) Discrete magnetic rod (DMR) simulation results for the five-M configuration ($\varepsilon = 10\%$). (B) Maximum θ_{mid} versus μ_1 and μ_2. (C) Comparison between DMR simulation results and theoretical predictions. The colormap represents the maximum θ_{mid} during the snapping process. (**D** and **E**) Representative experimental images of high-order modes. The images are selected to highlight key moments of the snapping behavior and do not correspond to uniform time intervals. The complete snapping processes are documented in real time in movies S8 and S9. (**F**) Normalized critical field B_c / B_3 versus $\mathcal{N}$ across various ε, revealing a quasi-linear universal scaling.

three regions: asymmetric ($\mathcal{N} = 3$), symmetric ($\mathcal{N} = 4$), and higher-order symmetric snapping ($\mathcal{N} = 6$). Each region corresponds to a minimum B_c, occurring near the respective region boundary. Normalizing the minimum B_c for different modes across various ε by the asymmetric mode (B_3) reveals a quasi-linear relationship between snapping order ($\mathcal{N}$) and normalized B_c / B_3 (Fig. 4F). This scaling establishes the connection across snapping modes and highlights the universality of M-interface designs. This relationship is reminiscent of classical Euler buckling, where critical loads scale quadratically with buckling order, albeit with different scaling behavior.

DISCUSSION

Our findings suggest a universal strategy for controlling snapping modes, with a particular focus on achieving symmetric snapping. Symmetric snapping requires a balance between driving forces to initiate snapping and resisting forces to suppress asymmetric modes. To validate this concept, we explored another classical bistable structure inspired by recent studies (*24*, *26*). As shown in Fig. 5 (A to C), a slender elastica, symmetrically clamped at an angle $\alpha = \pi / 12$rad and pre-buckled ($\varepsilon = 10\%$), was actuated using two methods: horizontal release (Fig. 5B) and end rotation (Fig. 5C). The midpoint rotation angle was monitored throughout the loading process for both horizontal release and end rotation methods, with results shown in Fig. 5 (B and C, middle). Both methods, involving only driving forces, resulted in asymmetric snapping under quasi-static conditions. Introducing a resisting force at the midpoint through coupled mechanical and magnetic loading enabled symmetric snapping (Fig. 5, B and C, right). The integration of magnetic actuation offers the added advantage of remote control. A more detailed study on the required magnitude of the resisting force is beyond the scope of this work and will be explored in future research. Given the similarities between the two methods and for ease of implementation, we selected the horizontal releasing method for further experimental validation. The experimental setup closely mirrors the simulation conditions described earlier. We prepared an HME-based bistable structure using the single-M design and carefully released the boundaries horizontally, both with and without an applied magnetic field. The experimental results, shown in movie S11, corroborate the simulation results in movie S10.

The distinct symmetric and asymmetric snapping modes offer substantial potential for various applications. Symmetric snapping, in particular, exhibits superior predictability in establishing reliable contact with substrates. For example, we designed a mechanical-magnetic snapping switch (Fig. 5D). Magnetic field–induced symmetric snapping successfully establishes stable contact, completing a circuit and lighting an light-emitting diode (LED) (Fig. 5E). In contrast, traditional mechanical loading induces asymmetric snapping, forming left-S or right-S configurations with inconsistent contacts that fail to activate the LED (Fig. 5, F and G). These findings highlight the advantages of symmetric snapping in achieving enhanced functionality across systems. Furthermore, the direction of the **B**-stimuli plays a crucial role in achieving symmetric snapping. In systems designed for symmetry, adjusting the orientation of the

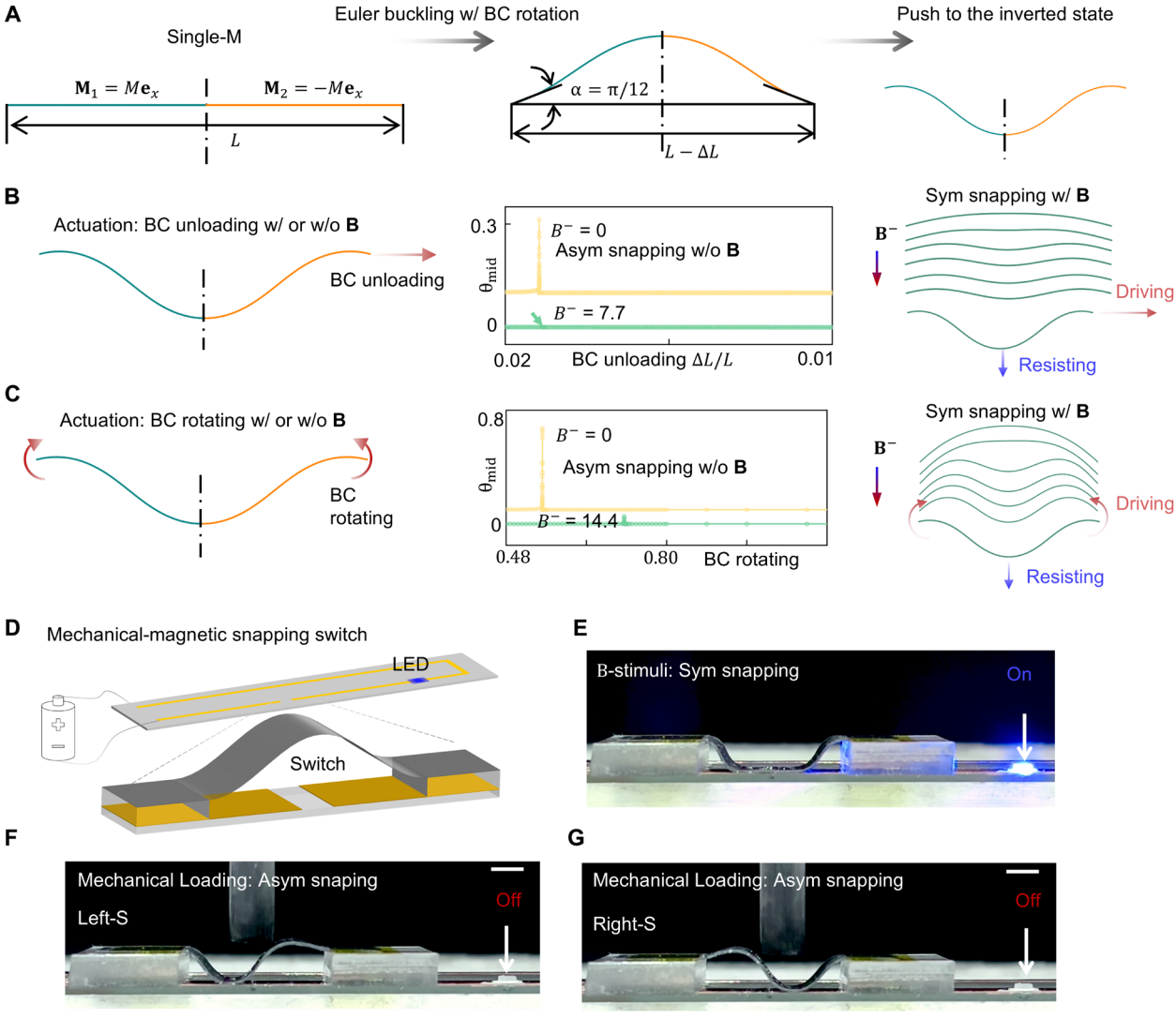

Fig. 5. Symmetric snapping in different systems and potential applications. (**A**) FEM simulation setup for a different classical bistable structure based on the single-M design. A clamped elastica with single-M design is used (left). Imposing pre-buckling ($\varepsilon = 10\,\%$) with symmetric end angles ($\alpha = \pi/12$) results in a bistable structure in natural state (middle). Subsequently pushing it to the other stable state gives the inverted state (right). (**B** and **C**) Two actuation methods were evaluated: horizontal release (B) and end rotation (C). The rotation angle θ_{mid} is plotted against the actuation process [(B) and (C), middle]. Horizontal release and end rotation result in asymmetric snapping under traditional mechanical loading ($B = 0$). Introducing a resisting force via magnetic field actuation enables symmetric snapping [(B) and (C), right]. See movie S10 for details. BC, boundary condition. (**D**) Schematic of the mechanical-magnetic snapping switch based on triple-M design. (**E** to **G**) Experimental results: magnetic field–induced symmetric snapping lights an light-emitting diode (LED) (E), and traditional mechanical loading induces asymmetric snapping, forming point contact that fails to activate the LED [(F) and (G)]. Scale bars, 3 mm. The images are selected to highlight key moments of the snapping behavior and do not correspond to uniform time intervals. The complete snapping processes are documented in real time in movie S12.

B-field alone can selectively trigger symmetric or asymmetric snapping. For symmetric snapping, the **B**-field must align with the $\mathbf{e}_z$ direction (i.e., the stimuli field must exhibit left-right symmetry), and μ (or μ_1 and μ_2 in five-M configuration) must fall within the symmetric snapping region. Conversely, asymmetric snapping can be initiated by significantly deviating the **B**-field direction from $\mathbf{e}_z$ in systems initially designed for symmetric mode. However, traditional designs or those with multiple M-interfaces that are not optimized for symmetric snapping will exhibit only asymmetric behavior, even when the B-field is aligned along the $\mathbf{e}_z$. This underscores the versatility and unique capabilities of our triple-M and five-M designs in achieving a wide range of snapping behaviors.

While this study focuses on quasi-static loading, investigating the dynamic behavior of these systems presents a compelling direction for future research (*37*–*40*). Furthermore, although our analysis centers on Euler buckling–based bistable structures, extending these findings to other bistable systems—such as rings (*41*, *42*), shells (*43*–*46*), and origami-based metamaterials (*47*–*49*)—is an intriguing prospect. These questions can open up exciting opportunities for future exploration.

MATERIALS AND METHODS

Method

Theoretical model

Details about the theoretical model, including Kirchhoff and FvK models, and discussions on the snapping order are presented in section S1.

Simulation methods

Given the equivalence between the magnetic field and point force models, we perform FEM simulations using the commercial software ABAQUS 6.14-4, which offers high computational efficiency. To complement traditional FEM simulations, we used the recently developed DMR method to investigate the dynamic behavior of the snapping process. Details about the simulation setups are presented in section S2.

Preparation of HME

The preparation of the hard ferromagnetic soft elastomers (HME) is briefly described as follows. HME comprises two components: hard MPs and soft elastomers. We selected NdFeB particles (5 μm) as MPs for their high coercivity and SEBS as the soft elastomer. SEBS particles were dissolved in toluene at a ratio of 5 g/20 ml. The MPs and dissolved SEBS were thoroughly mixed at a weight ratio of 2:1 using a homogenizer. The mixture was poured into a disk mold and left in a fume hood to volatilize the solvent, yielding an HME film with a thickness of ~1 mm. More details and data points that support the main figures are presented in section S3.

Supplementary Materials

The PDF file includes:

Supplementary Text
Figs. S1 to S12
Tables S1 to S6
Legends for movies S1 to S12

Other Supplementary Material for this manuscript includes the following:

Movies S1 to S12

REFERENCES AND NOTES

1. Y. Forterre, J. M. Skotheim, J. Dumais, L. Mahadevan, How the Venus flytrap snaps. *Nature* **433**, 421–425 (2005).
2. R. Sachse, A. Westermeier, M. Mylo, J. Nadasdi, M. Bischoff, T. Speck, S. Poppinga, Snapping mechanics of the Venus flytrap (*Dionaea muscipula*). *Proc. Natl. Acad. Sci. U.S.A.* **117**, 16035–16042 (2020).
3. S. O. Erbil, U. Hatipoglu, C. Yanik, M. Ghavami, A. B. Ari, M. Yuksel, M. S. Hanay, Full electrostatic control of nanomechanical buckling. *Phys. Rev. Lett.* **124**, 046101 (2020).
4. R. Bo, S. Xu, Y. Yang, Y. Zhang, Mechanically-guided 3D assembly for architected flexible electronics. *Chem. Rev.* **123**, 11137–11189 (2023).
5. Y. Wang, Q. Wang, M. Liu, Y. Qin, L. Cheng, O. Bolmin, M. Alleyne, A. Wissa, R. H. Baughman, D. Vella, S. Tawfick, Insect-scale jumping robots enabled by a dynamic buckling cascade. *Proc. Natl. Acad. Sci. U.S.A.* **120**, e2210651120 (2023).
6. D. Tang, C. Zhang, C. Pan, H. Hu, H. Sun, H. Dai, J. Fu, C. Majidi, P. Zhao, Bistable soft jumper capable of fast response and high takeoff velocity. *Sci. Robot.* **9**, eadm8484 (2024).
7. Y. Kim, J. van den Berg, A. J. Crosby, Autonomous snapping and jumping polymer gels. *Nat. Mater.* **20**, 1695–1701 (2021).
8. Q. Guo, Y. Sun, T. Zhang, S. Xie, X. Chen, Z. Zhang, H. Jiang, L. Yang, Bistable insect-scale jumpers with tunable energy barriers for multimodal locomotion. *Adv. Sci.* **11**, e2404404 (2024).
9. M. T. Flavin, K.-H. Ha, Z. Guo, S. Li, J.-T. Kim, T. Saxena, D. Simatos, F. Al-Najjar, Y. Mao, S. Bandapalli, C. Fan, D. Bai, Z. Zhang, Y. Zhang, E. Flavin, K. E. Madsen, Y. Huang, L. Emu, J. Zhao, J.-Y. Yoo, M. Park, J. Shin, A. G. Huang, H.-S. Shin, J. E. Colgate, Y. Huang, Z. Xie, H. Jiang, J. A. Rogers, Bioelastic state recovery for haptic sensory substitution. *Nature* **635**, 345–352 (2024).
10. C. Wang, Y. Wu, X. Dong, M. Armacki, M. Sitti, In situ sensing physiological properties of biological tissues using wireless miniature soft robots. *Sci. Adv.* **9**, eadg3988 (2023).
11. Z. Chen, S. Kong, Y. He, S. Chen, W. Wang, L. Jin, S. Zhang, Y. Hong, L. Pan, H. Wu, Y. Xie, C. Linghu, Z. Mao, Z. Yang, C. H. Chan, J. Song, J. Lu, A magnet-driven soft bistable actuator. *Adv. Funct. Mater.* **34**, 2311498 (2024).
12. C. Li, H. Luo, J. Song, Magnetically driven non-contact transfer printing based on a bi-stable elastomeric stamp. *Adv. Mater. Technol.* **6**, 2100335 (2021).
13. Y. Ma, X. Feng, J. A. Rogers, Y. Huang, Y. Zhang, Design and application of 'J-shaped' stress–strain behavior in stretchable electronics: A review. *Lab Chip* **17**, 1689–1704 (2017).
14. S. An, Y. Cao, H. Jiang, A mechanically robust and facile shape morphing using tensile-induced buckling. *Sci. Adv.* **10**, eado8431 (2024).
15. X. Zhang, Y. Wang, Z. Tian, M. Samri, K. Moh, R. M. McMeeking, R. Hensel, E. Arzt, A bioinspired snap-through metastructure for manipulating micro-objects. *Sci. Adv.* **8**, eadd4768 (2022).
16. S. Yang, P. Sharma, A tutorial on the stability and bifurcation analysis of the electromechanical behaviour of soft materials. *Appl. Mech. Rev.* **75**, (2023).
17. K. Tan, L. Chen, S. Yang, Q. Deng, Snap-through instability-driven enhancement of magnetoelectric coupling in soft electrets. *J. Mech. Phys. Solids* **196**, 106043 (2025).
18. A. Pandey, D. E. Moulton, D. Vella, D. P. Holmes, Dynamics of snapping beams and jumping poppers. *EPL* **105**, 24001 (2014).
19. W. Huang, C. Ma, L. Qin, Snap-through behaviors of a pre-deformed ribbon under midpoint loadings. *Int. J. Solids Struct.* **232**, 111184 (2021).
20. Y. Zhang, Y. Ma, J. Yu, H. Gao, Non-contact actuated snap-through buckling of a pre-buckled bistable hard-magnetic elastica. *Int. J. Solids Struct.* **281**, 112413 (2023).
21. F. Zhang, S. Li, Z. Shen, X. Cheng, Z. Xue, H. Zhang, H. Song, K. Bai, D. Yan, H. Wang, Y. Zhang, Y. Huang, Rapidly deployable and morphable 3D mesostructures with applications in multimodal biomedical devices. *Proc. Natl. Acad. Sci. U.S.A.* **118**, e2026414118 (2021).
22. A. Abbasi, T. G. Sano, D. Yan, P. M. Reis, Snap buckling of bistable beams under combined mechanical and magnetic loading. *Philos. Trans. R. Soc. Math. Phys. Eng. Sci.* **381**, 20220029 (2023).
23. M. R. Shankar, M. L. Smith, V. P. Tondiglia, K. M. Lee, M. E. McConney, D. H. Wang, L.-S. Tan, T. J. White, Contactless, photoinitiated snap-through in azobenzene-functionalized polymers. *Proc. Natl. Acad. Sci. U.S.A.* **110**, 18792–18797 (2013).
24. B. Radisson, E. Kanso, Elastic snap-through instabilities are governed by geometric symmetries. *Phys. Rev. Lett.* **130**, 236102 (2023).
25. T. G. Sano, H. Wada, Snap-buckling in asymmetrically constrained elastic strips. *Phys. Rev. E* **97**, 013002 (2018).
26. Q. Wang, A. Giudici, W. Huang, Y. Wang, M. Liu, S. Tawfick, D. Vella, Transient amplification of broken symmetry in elastic snap-through. *Phys. Rev. Lett.* **132**, 267201 (2024).
27. Y. Kim, H. Yuk, R. Zhao, S. A. Chester, X. Zhao, Printing ferromagnetic domains for untethered fast-transforming soft materials. *Nature* **558**, 274–279 (2018).
28. R. Zhao, Y. Kim, S. A. Chester, P. Sharma, X. Zhao, Mechanics of hard-magnetic soft materials. *J. Mech. Phys. Solids* **124**, 244–263 (2019).
29. L. Wang, Y. Kim, C. F. Guo, X. Zhao, Hard-magnetic elastica. *J. Mech. Phys. Solids* **142**, 104045 (2020).
30. S. Wu, W. Hu, Q. Ze, M. Sitti, R. Zhao, Multifunctional magnetic soft composites: A review. *Multifunct. Mater.* **3**, 042003 (2020).
31. L. Wang, D. Zheng, P. Harker, A. B. Patel, C. F. Guo, X. Zhao, Evolutionary design of magnetic soft continuum robots. *Proc. Natl. Acad. Sci. U.S.A.* **118**, e2021922118 (2021).
32. D. Mukherjee, M. Rambausek, K. Danas, An explicit dissipative model for isotropic hard magnetorheological elastomers. *J. Mech. Phys. Solids* **151**, 104361 (2021).
33. Y. Kim, X. Zhao, Magnetic soft materials and robots. *Chem. Rev.* **122**, 5317–5364 (2022).
34. D. Yan, A. Abbasi, P. M. Reis, A comprehensive framework for hard-magnetic beams: Reduced-order theory, 3D simulations, and experiments. *Int. J. Solids Struct.* **257**, 111319 (2022).
35. W. Huang, M. Liu, K. J. Hsia, A discrete model for the geometrically nonlinear mechanics of hard-magnetic slender structures. *Extreme Mech. Lett.* **59**, 101977 (2023).
36. L. Chen, K. Tan, S. Yang, Q. Deng, Evoking the snap-through instability in hard-magnetic soft materials: Rapid actuation and giant deformation. *Int. J. Solids Struct.* **246–247**, 111607 (2022).
37. M. Gomez, D. E. Moulton, D. Vella, Critical slowing down in purely elastic 'snap-through' instabilities. *Nat. Phys.* **13**, 142–145 (2017).
38. M. Liu, M. Gomez, D. Vella, Delayed bifurcation in elastic snap-through instabilities. *J. Mech. Phys. Solids* **151**, 104386 (2021).
39. B. Radisson, E. Kanso, Dynamic behavior of elastic strips near shape transitions. *Phys. Rev. E* **107**, 065001 (2023).
40. E. Y. Urbach, E. Efrati, Predicting delayed instabilities in viscoelastic solids. *Sci. Adv.* **6**, eabb2948 (2020).
41. L. Lu, S. Leanza, J. Dai, J. W. Hutchinson, R. R. Zhao, Multistability of segmented rings by programming natural curvature. *Proc. Natl. Acad. Sci. U.S.A.* **121**, e2405744121 (2024).
42. W. Huang, T. Yu, K. J. Hsia, S. Adriaenssens, M. Liu, Integration of kinks and creases enables tunable folding in meta-ribbons. *Matter* **7**, 3007–3023 (2024).
43. D. P. Holmes, Elasticity and stability of shape-shifting structures. *Curr. Opin. Colloid Interface Sci.* **40**, 118–137 (2019).

44. A. Abbasi, T. Chen, B. F. G. Aymon, P. M. Reis, Leveraging the snap buckling of bistable magnetic shells to design a refreshable braille dot. *Adv. Mater. Technol.* **9**, 2301344 (2024).
45. W. Huang, Z. Liu, M. Liu, K. J. Hsia, Snap-through eversion of axisymmetric shells under contact indentation. *Proc. R. Soc. Math. Phys. Eng. Sci.* **480**, 20240303 (2024).
46. X. Cheng, Z. Fan, S. Yao, T. Jin, Z. Lv, Y. Lan, R. Bo, Y. Chen, F. Zhang, Z. Shen, H. Wan, Y. Huang, Y. Zhang, Programming 3D curved mesosurfaces using microlattice designs. *Science* **379**, 1225–1232 (2023).
47. Z. Zhai, L. Wu, H. Jiang, Mechanical metamaterials based on origami and kirigami. *Appl. Phys. Rev.* **8**, 041319 (2021).
48. L. Lu, S. Leanza, R. R. Zhao, Origami with rotational symmetry: A review on their mechanics and design. *Appl. Mech. Rev.* **75**, 050801 (2023).
49. D. Misseroni, P. P. Pratapa, K. Liu, B. Kresling, Y. Chen, C. Daraio, G. H. Paulino, Origami engineering. *Nat. Rev. Methods Primers* **4**, 40 (2024).

Acknowledgments: We thank C. Cao, Y. Liu, X. Yang, and X. Wang for assistance in preparing the materials. **Funding:** The work is supported by a start-up grant from Tsinghua University and Singapore National Research Fellowship (NRF-NRFF11-2019-0004). **Author contributions:** Conceptualization: Y.Z. and H.G. Methodology: Y.Z. investigation: Y.Z., W.H., and M.L. Formal analysis: Y.Z., W.H., M.L., J.Y., and H.G. Visualization: Y.Z. Supervision: J.Y. and H.G. Funding acquisition: J.Y. and H.G. Writing—original draft: Y.Z. Writing—review and editing: Y.Z., W.H., M.L., J.Y., and H.G. **Competing interests:** The authors declare that they have no competing interests. **Data and materials availability:** All data needed to evaluate the conclusions in the paper are present in the paper and/or the Supplementary Materials.

Submitted 21 January 2025
Accepted 9 April 2025
Published 14 May 2025
10.1126/sciadv.adw1259